Received Signal Strength Visible Light Positioning-based Precision Drone Landing System

Sander Bastiaens, Jens Mommerency, Kenneth Deprez, Wout Joseph and David Plets
INTEC - WAVES, Ghent University/imec, Ghent, Belgium
Email: Sander.Bastiaens@UGent.be

***Abstract*—The next-generation automated inventory management solution revolves around unmanned aerial drones that operate without any human intervention, including during (wireless) charging. As the inductive power transfer system's efficiency depends on its coil alignment, a precision landing system is required that is lightweight, accurate, and of low-cost. This manuscript demonstrates the potential of received signal strength (RSS) Visible Light Positioning (VLP) with a single photodiode (PD), which is inherently lightweight. A landing system is proposed, in which a PD-equipped drone self-localises with respect to light-emitting diodes (LEDs) that are integrated into the landing zone. The LEDs are furthermore sequentially strung together to cut costs, thereby forming a LED *strip*. Automated measurements characterise the particular (propagation) challenges and the positioning performance of 3D VLP on a small scale, when mimicking drone landing on a flat surface or in a commercial funnel. For the flat surface, a 50 Hz update rate and a vertical range up to 1 meter, the target of a third quartile VLP-only positioning error bounded by 3.5 cm is attained with multilateration and a 6-element LED strip. The presence of the reflections-inducing drone funnel degrades the positioning performance significantly. However, a sufficient accuracy can still be reached. Both configurations exhibit larger errors close to the landing zone.**

***Index Terms*—Visible Light Positioning, VLP, 3D, Received Signal Strength, RSS, Photodiode, Precision landing, Positioning**

I. Introduction

Within the scope of Industry 4.0, automating the physical subtask of stock taking, alleviates both the substantial manual labour cost and injury risk, and dispenses with the stock level inaccuracies caused by human errors. Drone technology innovations have predestined the use of unmanned aerial vehicles (UAVs) for the indoor automatic stocktaking purpose. With the drones' flight time limited to 10 – 60 minutes [1], depending on the drone type, load and battery pack specifications, an optimised stock picking requires the efficient charging of the drones between the flights. From an economics standpoint, rather than resorting to a manual intervention (e.g. of swapping out the batteries), an automated (wireless) power transfer system is strived for.

This work was executed within *InWareDrones*, a research project bringing together academic researchers and industry partners. The *InWareDrones* project was co-financed by imec (iMinds) and received project support from Flanders Innovation & Entrepreneurship. The authors thank DroneMatrix for providing the drone (funnel).

978-1-6654-0402-0/21/$31.00 ©2021 IEEE

In inductive wireless power transfer systems, the charging efficiency depends on the degree of alignment between the primary charging coil of the drone charging station and the (lightweight) secondary coil on-board the drone [2]. Automated battery replacement solutions require proper alignment as well [3]. Whereas in literature, (mechanical) methods are proposed to mitigate the misalignment [2]–[4], the drone precisely landing in or on the designated charging station is of that importance that the drone is fitted with a dedicated localisation system for landing.

Perspective landing systems should ideally enable typical positioning accuracies below $3.5\ \mathrm{cm}$, or below $10\ \mathrm{cm}$ when featuring in conjunction with guidance structures, such as a drone funnel. Current drone landing systems rely hereto on either a visible light capturing or an infrared (IR)-sensitive camera receiver. By localising with respect to (non)fiducial markers on/near the target location, (sub)decimetre accurate landing can be ensured with additional sensors (e.g. a one-dimensional LIDAR) aiding in compensating and improving vision technology's drift and distance estimation respectively [5]–[7]. IR systems, such as the IR-LOCK's MarkOne[1] (Pixy) Sensor and Beacon combination, can make use of IR LED transmitters to boost both the range and accuracy with respect to the infrastructure-light solution [8], [9].

The disadvantages of both camera-based systems mainly lie in that (1) their weight is detrimental for the drone's airtime and (2) they require significant computational resources.

Positioning based on signals embedded in the visible light originating from Light-Emitting Diodes (LEDs), i.e. Visible Light Positioning, has been gaining prominence for having the potential for delivering (sub)decimetre-accurate localisation at a limited cost [10]–[12]. As received signal strength (RSS)-based VLP only needs a single photodiode (PD), a sensitive 'single pixel', its receiver can be cheap, lightweight and simple/fast (by not requiring the extensive processing resources of camera systems). All of which are prerequisites for precision drone landing.

This manuscript demonstrates for the first time the aptitude of single photodiode-based RSS VLP for highly-accurate precision landing. In the proposed system, a photodiode receiver is mounted on the drone to serve the purpose of landing in/on a designated zone, namely the docking station. When the drone ventures in the neighbourhood of the docking station, the drone

[1] https://irlock.com/collections/ir-markers

(a) (b)

Fig. 1. Visualisation of the (a) flat surface and (b) drone funnel landing zone with the measurement setup (i.a. the Velmex slider system) present.

localises itself with respect to the LED transmitters that are integrated into the landing zone.

To refrain from needing a VLP driver per LED and incurring the associated cost, each LED's modulation frequency and supply are derived from a sole LED driver i.e. the LEDs form a LED *strip*. By having each LED transmit a square pulse train with a base frequency that is a unique power 2 of a ground frequency, in accordance with the (de)modulation scheme of [13], a simple frequency halver (or binary divider) circuit suffices to generate each LEDs' driving current. In order to optimally cover a landing range presupposed up to $2\ \mathrm{m}$ high (a practical specification), the LED strip circuit is able to feature both quasi-omnidirectional and (highly-)directive LEDs.

The 3D positioning accuracy of this system when one-shot (without keeping state) localising at $50\ \mathrm{Hz}$ with either a multi-lateration, a model-based fingerprinting or a hybrid positioning algorithm, is measured by installing a commercial PD on a 3D slider system. The sliders are placed in front of the target zone, with both landing on a flat area and in a commercial drone funnel considered. This manuscript contains a discussion on a cost-effective and lightweight receiver prototype.

The main contributions of this paper can be condensed to:

- The design of a frequency divider-based LED strip for cost-effective VLP.
- An experimental characterisation of the propagation and 3D VLP accuracy in the neighbourhood of a drone landing site or metallic funnel.
- A discussion on the aptitude of VLP for drone landing, encompassing a case-study of a drone-integrated VLP solution.

II. Materials and Methods

A. LED strip

As stated in the introduction, the drone navigates itself with respect to the docking station equipped with intelligently-placed LEDs. Fig. 1 shows two LED-equipped landing zones.

By making use of square waves-based frequency division multiple access (FDMA) intensity modulation [13], the overall system cost and complexity can be minimised on account of being able to sequentially string together the LEDs to form a LED strip. In addition to the LED strip only requiring a single supply, each individual LED module's even order harmonic modulation frequency $f_{c,i}$ ($i = 1..N$, with N the number of LEDs) can be furthermore derived from a sole pulse-width modulation (PWM) generator (with frequency $f_{c,N+1}$) by successively halving $f_{c,N+1}$ using a simple frequency (or clock) divider circuit. In practice, the N^{th} LED's frequency halver can be bypassed, so that the PWM frequency is $f_{c,N}$.

Fig. 2 (a) depicts a schematic representation of the modular prototype LED strip, whilst Fig. 2 (b) zooms in on the frequency divider building block. In each LED module, the output voltage of the (ON Semiconductor NL17SZ74USG[2]) D flip-flop-based frequency divider is applied at the gate of an N-Channel MOSFET (ON Semiconductor TR5198NLT1G[3]), itself driving the LED.

To cover the $2\ \mathrm{m}$ operating range, a LED module can be configured to support either (a) a LUMILEDS LUXEON L2C5-40HG1203E0900[4] chip-on-board (COB) LED (on top of a heat sink) meant for the larger drone-distances or (b) a CREE XLamp XP-E-WHT-L1-0000-00AE5E[5] surface-mounted-device (SMD) LED designated with the intention of precision manoeuvring close to the designated landing spot. The LED driving currents respectively amount to approximately $250\ \mathrm{mA}$ and $300\ \mathrm{mA}$. The SMD LEDs are fitted with a LEDiL CA11663_HEIDI-RS[6] lens to increase their directionality, i.e. their Lambertian order (to $m_i = 284.2$).

Both LED sub-strings comprise the same functional circuit, differ in the edge components (e.g. supply voltage divider resistors) and operate simultaneously or independently (when disassembled). The LED strip interfaces with the mains via the TDK-Lambda LS75-36[7] AC/DC supply regulator (adjusted to $38\ \mathrm{V}$), or when only SMD modules are utilised via the $5\ \mathrm{V}$ Traco Power TXM 015-105[8].

B. Demodulation and Localisation Algorithms

1) Demodulation: At the drone, the single photodiode's measured time domain photocurrent signal $I_{PD}(t)$ is demodulated into per LED contributions $I_{PD,i}$ ($i = 1..N$) via the standard fast Fourier transform (FFT)-based procedure [13], [14]. To cope with a potentially non-nominal or (minimally) unstable LED strip frequency, a peak detection in the $2\Delta f_i$ neighbourhood of the nominal modulation frequency $f_{c,i}$, i.e. $[f_{c,i} - \Delta f_i, f_{c,i} + \Delta f_i]$, with $\Delta f_i = {}^{f_{c,i}}/_{100}$, is added to increase the demodulation's robustness.

2) Propagation Model and Calibration: The next Section II-B3's positioning algorithms employ the first order Line-of-Sight (LOS) IR-based propagation models of Kahn et al. [15]. For description details refer to previous work [14]. Besides a priori charting the LED locations, for each LED (LED_i), the product of the wavelength-weighted (M) receiver responsivity (R_p) and radiant flux ($P_{t,i}$), i.e. $M \cdot P_{t,i} \cdot R_p$ is calibrated too [14].

[2]https://www.onsemi.com/pdf/datasheet/nl17sz74-d.pdf
[3]https://www.onsemi.com/pdf/datasheet/ntr5198nl-d.pdf
[4]https://www.lumileds.com/products/cob-leds/luxeon-cob/
[5]https://cree-led.com/products/xlamp-leds-discrete/xlamp-xp-e
[6]https://www.ledil.com/data/prod/Heidi/11663/11663-ds.pdf
[7]https://product.tdk.com/en/system/files?file=dam/doc/product/power/switching-power/ac-dc-converter/catalog/ls25-150_e.pdf
[8]https://www.tracopower.com/int/model/txm-015-105

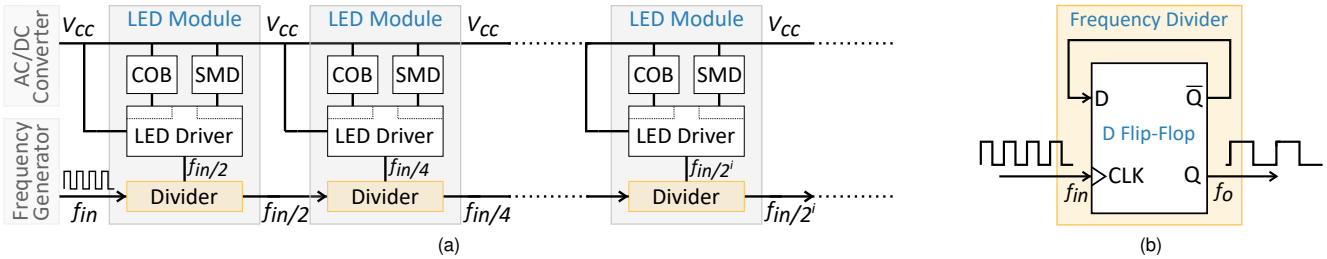

Fig. 2. Schematic representation of (a) the LED strip and (b) its frequency divider building block.

3) Positioning Algorithms: Given a subset of $\{I_{PD,i}\}$ [14], the channel model and the accurately known LED locations $\hat{\mathbf{x}}_S = (x_{S,i}, y_{S,i}, 0)$, each considered positioning algorithm (with their individually optimised $\{I_{PD,i}\}$ subset) computes a receiver location estimate $\hat{\mathbf{x}}$ of the real location $\mathbf{x}$.

In 2D localisation and in the absence of receiver tilt, *model-based fingerprinting (MBF)* [14] offers a more viable alternative for the cumbersome manual fingerprinting process by computing the fingerprints from the channel model (instead of measuring them). Unfortunately, for drone landing, the fingerprints need to be matched across 5 dimensions[9], i.e. in 3D space and over the azimuthal and inclination angles that describe the tilt of the receiver normal. Even on the limited scale found in drone landing, fingerprint storage and matching latency quickly become infeasible, certainly due to the limited resources available for the landing system on-drone. Assuming the VLP receiver's active surface to remain (relatively) parallel with the ground, for instance when either the drone hovers stably before perpendicularly descending or when a stabiliser (gimbal) is employed, 2D *MBF* should suffice to provide the accurate localisation required. The granularity of the *MBF* propagation model is set to 2.5 cm.

Closed-form least-squares multilateration does not require the storage or the computation resources *MBF* does. Multilateration inverts the channel model to relate $\{I_{PD,i}\}$ to the set of distances between the PD and each LED $\{d_i\}$ and then to $\hat{\mathbf{x}}$. The invertibility-requirement imposes stringent restrictions on the propagation model [14], which in practice means that: (a) the LED's radiation pattern needs to be approximated to that of an ideal Lambertian point source, and (b) the non-line-of-sight (NLOS) effects cannot be accurately modelled. In [16], Plets et al. proposed a more robust 3D multilateration alternative, referred to with *MLT* here, which is still of a low complexity and overhead by relying on a height-dependent cost function and an iterative application of 2D multilateration. When keeping state, the height candidate set, here $[0\text{ m}, 2\text{ m}]$ in steps of 1 cm, can be vastly reduced based on the previous receiver height.

[9]Obtaining the propagation model due to computation (in *MBF*) or measurement (in manual fingerprinting) for discrete tilt values is, though time-consuming, a feasible off-line process. By utilising sparse fingerprinting matching techniques, both may be useful for highly-accurate 3D VLP drone landing in a stable small-scale environment. The measurement setup described in Section II-C in tandem with a tilting platform would be an exemplar system to measure the required fingerprints.

In the result section, it will be determined to which extent (or height) *MLT* is able to supply accurate positioning, if and when correspondingly *MBF* or manual fingerprinting needs to be switched to (thereby forming a hybrid algorithm).

4) Evaluation Metric: The 3D positioning accuracy is evaluated in terms of the 75$^{\text{th}}$ percentile p_{75} of the positioning error. The latter equals the Euclidean distance between the actual $\mathbf{x}$ and estimated $\hat{\mathbf{x}}$ position. Tailored to the landing use case, the evaluation space is defined as a rectangular frustum, widening from a 10 cm-sided square at the landing height to a 1 m-sided square 1 m higher up. At vertical distances exceeding 1 m, the evaluation volume is kept 1 m wide.

C. Measurement Setups

In WAVES' VLP lab [14], the p_{75} localisation accuracy is assessed for various configurations that mimic a perpendicular drone landing: on a flat surface (*FS*) with (a) solely a 6-element COB LED strip and (b) with both a 6-element COB and SMD LED strip integrated in a (double) triangular structure; in the commercial landing funnel of DroneMatrix[10] (*DM*) equipped with (c) a shrunken version of (b) and with (d) 5 COBs placed in a skewed quadrilateral with a central LED. All the configurations' LED coordinates are represented in Fig. 3. The LED constellations are selected as to not form lines or circles when only employing a 4-element subset of the $\{I_{PD,i}\}$, which would otherwise hinder 3D positioning [16]. Although both subsystems can technically feature in a single LED strip, the limited frequency range available, coerces to utilise 2 separate LED strips, here with ground frequencies 500 Hz and 300 Hz.

Fig. 1 depicts the flat surface as well as the drone funnel configuration under test. Equipped with the Thorlabs PDA36A2[11] (set to a $4.75 \cdot 10^3$ V/A transimpedance gain) and a National Instrument USB-6212 DAQ device[12], a Velmex 3D slider system [14], which is placed in front of the landing zone, traverses a 1 m^3 volume with a predefined granularity (default value 5 cm) to measure $I_{PD}(t)$ with $f_S/50$ samples at an $f_S = 255$ kHz ($f_S = 123.4$ kHz for *DM* with 5 COBs) sample rate. After demodulation (into $I_{PD,i}$), at 50 Hz, a location estimate is computed with the positioning algorithms from Section II-B3. However, only the data in the evaluation zone is considered in calculating the p_{75}. The LEDs' $M \cdot P_{t,i} \cdot R_p$

[10]https://www.dronematrix.eu/
[11]https://www.thorlabs.com/thorproduct.cfm?partnumber=PDA36A2
[12]https://www.ni.com/pdf/manuals/375196d.pdf

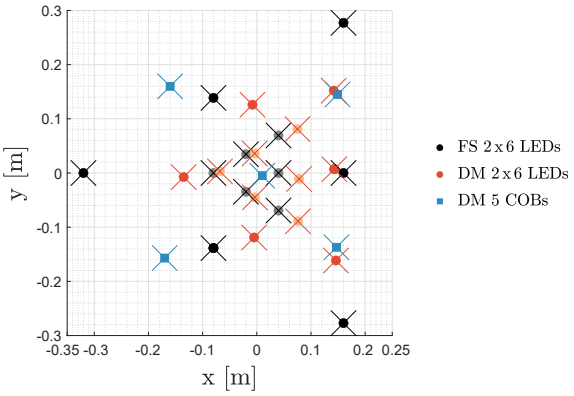

Fig. 3. Distribution of the LEDs for the various drone landing configurations. When present, the SMD LED locations are visualised in lighter shades compared to their COB counterparts.

is calibrated on the grid point closest to the projection of the LED's coordinate on the 2D measurement plane parallel to the LED plane at the nearest available height (between planes) to 75 cm, and $f_{c,N_{COB}}/f_{c,N_{SMD}}$ (with N_{COB} and N_{SMD} the number of COB and SMD LEDs, respectively) are generated by a function generator.

III. Experimental Results

A. Electrical Performance of the LED strip

The 6-element LED strips' 3 dB bandwidth (BW) is measured with the PDA36A2 to equal approximately 200 kHz and 16 kHz for the SMD and COB strip, respectively. With an $f_{c,N+1} = 32$ kHz, neither strip showed a non-zero standard deviation on $f_{c,1}$. The frequency signal of the last COB module does exhibit a noticeable overshoot with a maximal amplitude of about 10% over a duration of 17.7 µs. Although, in [17], it was shown that overshoot degrades the accuracy of RSS-based VLP, the contributions at the intermediate LEDs (of the strip) have similar characteristics, which in turn facilitates their (partly) out-calibration.

B. Propagation near the LED

Prior to the localisation experiments, the mid-field (compared to traditional VLP) LED radiation pattern is measured to study to which extent it diverges from that of the ideal Lambertian radiation point source (and the datasheet pattern). Fig. 4 (a) and (b) show at first glance the concentric circles accustomed to when plotting the spatial distribution of $I_{PD,i}$ of near-Lambertian point source radiators. However, when performing $M \cdot P_{t,i} \cdot R_p$ calibration over an increasing vertical distance (i.e. height or z-slider position) to the LED, $M \cdot P_{t,i} \cdot R_p$ only converges to within 1% of its 'far' field value, at 50 cm, at a 15 cm LED-PD distance. In other words, nearing the LED closer than 15 cm increasingly invalidates the point source approximation. It is important to note that this bound is an approximation, due to the limited measurement granularity and possible inaccuracies in the measured LED location (measured by hand).

MBF is able to incorporate an arbitrary radiation pattern. Deriving a point-source approximation of the measured radiation pattern (normalised in the visualisation of Fig. 4 (e)) allows comparing with localisation centred around the Lambertian approximation. Discrepancies between both are noticeable for polar radiation angles exceeding 45°.

C. Inter-LED interference with the LED strip(s)

The cost-effectiveness of stringing LEDs together does come at a disadvantage that is remarked when comparing the spatial distribution of the standard deviation $\sigma(I_{PD,i})$ of the RSS values $I_{PD,i}$ of a single LED with the one of LED 3 (indicated in black in Fig. 3) of the 6-element COB LED strip in the flat surface configuration (Fig. 5 (a)), displayed in Fig. 4 (c)/(d) and Fig. 5 (b)-(d), respectively. $\sigma(I_{PD,i})$ is computed per grid point over 20 measurements.

Whereas the former's $\sigma(I_{PD,i})$ (Fig. 4) fits well with the standard shot and thermal noise combination [18] (with small additional effects at close range), the latter's $\sigma(I_{PD,i})$ (Fig. 5) is dominated by the precursor LEDs in the LED strip. Well-modelling the LED strips' $\sigma(I_{PD,i})$ hence requires adding intersymbol interference terms to the noise variance computation $\sigma^2(I_{PD,i})$ [18]. These interference terms are proportional to $(I_{PD,j})^2$, $j = (i+1)\,..\,N$, with the proportionality factor of the immediate predecessor exceeding that of the other predecessors. $\sigma(I_{PD,i})$ also exhibits smaller influences of the successor LEDs.

Besides intra-LED-strip-interference, inter-LED-strip interference manifests itself as well, as attested by Fig. 5 (a) and (e). Fig. 5 (e) shows the bias errors introduced by in-frequency-neighbouring SMD LEDs in the $I_{PD,i}$ distribution of a COB LED as a consequence of non-ideal (de)modulation effects (such as overshoot).

D. Localisation

With the particularities of the landing use case characterised, in terms of the small-scale and LED strip-based propagation, this Section III-D treats the associated positioning performance of RSS-based VLP in the presence of the landing zone configurations outlined in Section II-C. For each configuration, the height-dependence of the p_{75} is averaged over 20 50 Hz landing experiments.

1) Flat Surface (FS) with 6 COB LEDs: Fig. 6 depicts the height-p_{75} curves to be convex, when localising near the 6 COBs-counting LED strip triangularly integrated into the flat surface landing zone. Significant errors are found close (< 10 cm) to the LEDs, where VLP-only positioning proves difficult. Multilateration (*MLT*) is shown to be viable for landing in the $]23\text{ cm}, 90\text{ cm}[$ height range, where a $p_{75} \leq 3.5$ cm is attained. Interestingly, most of *MLT*'s error is found for its z-component, shown by Fig. 6's light blue curve designated by *MLT* - E_h. Whereas *MBF* assuming a Lambertian radiation pattern (*MBF* - *LAMB*) scores comparably to *MLT*, *MBF* with for each LED the measured radiation pattern of Section III-B (referred to with *MBF* - *RADP*) is able to ameliorate the p_{75}

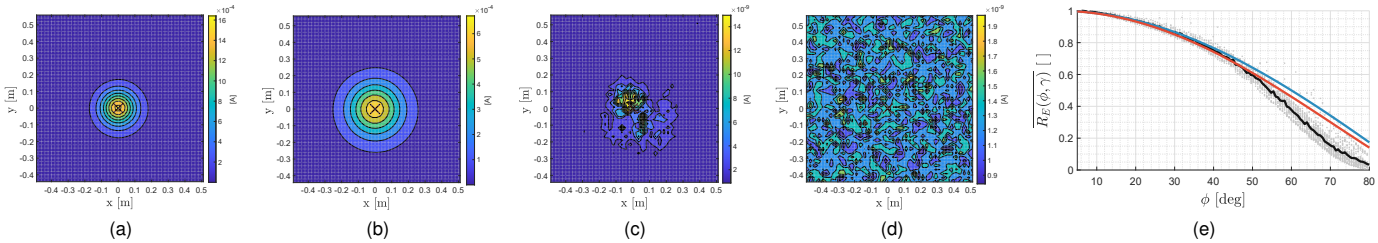

Fig. 4. A single LED's $I_{PD,1}$ at approximately (a) 10 cm and (b) 20 cm, and $\sigma\left(I_{PD,1}\right)$ at approximately (c) 10 cm and (d) 50 cm vertical distance from the LED. The LED's coordinate is indicated in black. Subfigure (e) shows the derived normalised radiation pattern measurement data, with the black, blue and red curve indicating the overall median of the data, the ideal $m = 1$ and best-fitting Lambertian order [14], respectively.

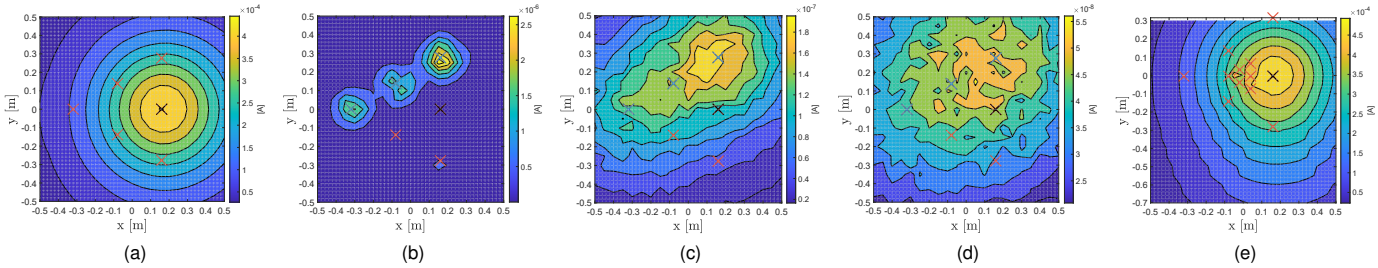

Fig. 5. The spatial distribution of LED strip member $i = 3$'s (a) $I_{PD,3}$ approx. 50 cm and $\sigma\left(I_{PD,3}\right)$ approx. (b) 10 cm, (c) 50 cm and (d) 1 m above the flat surface landing zone equipped with the 6-element COB LED strip, while (e) displays $I_{PD,3}$ when both LED strips are featured. The LED coordinates are visualised in red, with LED 3 highlighted in black. In (b)-(d), LED 3's predecessors are overpainted in blue.

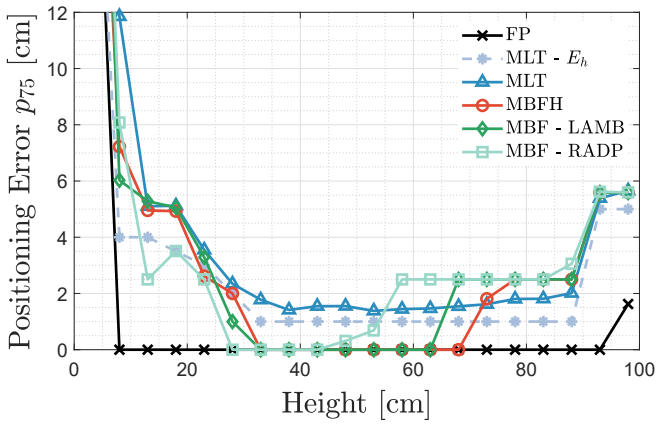

Fig. 6. Experimentally measured p_{75} over the receiver height for various positioning algorithms, in the presence of the 6 COB LED strip integrated into the flat surface landing zone in a triangular fashion (see Fig. 3).

closer to the LED. Herefrom, it can be concluded that employing a more thoroughly characterised, preferably a non-point, radiation pattern should enable more accurate localisation. The current *MBF* p_{75} does not warrant its additional complexity, compared to *MLT*. A *MLT-MBF* hybrid form (*MBFH*, shown in red), which performs *MBF* constrained to the immediate (10 cm) vicinity of *MLT*'s estimate, only makes sense close to the LED when *MBF* is better tuned.

Furthermore, Fig. 6 holds a black reference curve that depicts the p_{75} found when performing manual fingerprinting (*FP*) with the per grid point averaged $I_{PD,i}$ fingerprints. It shows the best attainable p_{75} for VLP and should correspond to *MBF*'s p_{75}, i.e. were it not for bias errors in the latter's propagation model introduced by i.a. mismatches between the measured and modelled LED coordinates, the presence of small LED tilts and/or an imperfectly modelled LED radiation pattern. It needs to be remarked that for manual fingerprinting the evaluation is performed on the exact 3D positions where the fingerprints are collected. The grid is furthermore coarsely (i.e. 5 cm) spread. Thus, as the drone can be situated in between grid points, the p_{75} in practice will be shifted upward. The *FP* curve, as a lower bound, does show VLP's tremendous potential. However, close to the landing zone improvements are still needed.

2) Flat Surface with 2x6 LEDs: The black curve in Fig. 7 (a) shows that these improvements can be obtained by introducing an additional LED strip with directive LEDs (see Fig. 1(a)), which have the purpose of adding larger gradients in *FP*'s cost function close to the LEDs. Fig. 7 (a) displays that the p_{75} values appertaining to *MLT* and the *MBF* types reduce as well (at heights below 15 cm), when compared to Fig. 6. This reduction is, however, not (entirely) the result of the expected SMD LED propagation contributions themselves, but also of the undesired (intra- and) inter-LED-strip interference induced (Section III-C). Rerunning *FP* (and *MBF - RADP*) on the set of $\{I_{PD,i}\}$ belonging to the COB LEDs, i.e. where the SMD LEDs' $\{I_{PD,i}\}$ are omitted from, substantiates this claim. The associated p_{75} curves, designated with '-COB' suffix, display smaller errors at the lower heights than their counterparts.

Furthermore, the interference-induced bias in the $I_{PD,i}$ distribution significantly augments the p_{75} of *MLT* and the *MBF*

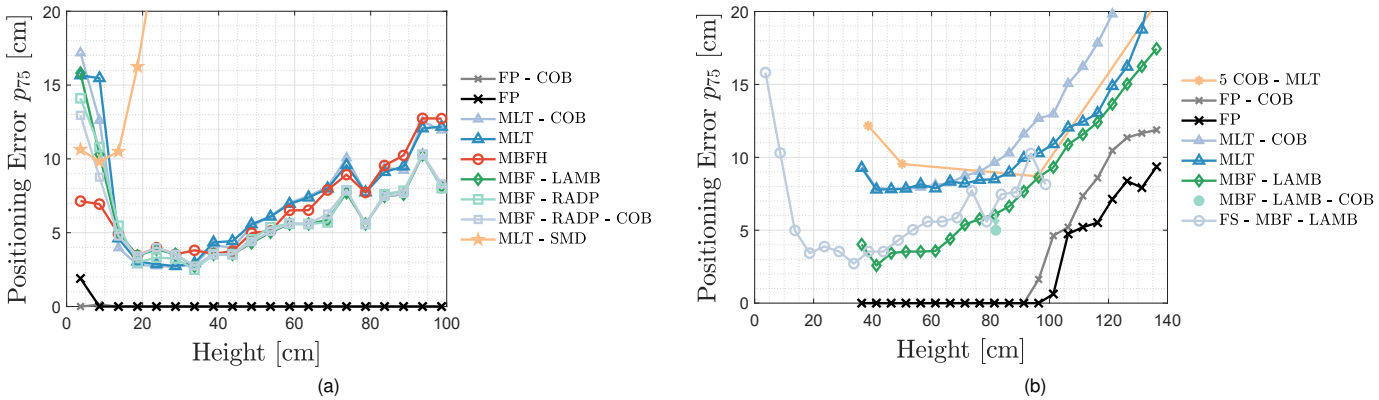

Fig. 7. The height-p_{75} curves for multilateration- and manual/model-based fingerprinting-based positioning in the 2 landing situations visualised in Fig. 1.

algorithms for an increasing perpendicular distance between the drone and the landing zone. The limited viable range with $p_{75} < 3.5\,\text{cm}$ compels the use of manual fingerprinting to be able to support precision landing with both LED strips. Overall, the SMD LED strip worsens the performance in its current form, and should hence not be employed for precision landing. Also, as was for the previous experiment, *MBF - RADP* distinctively outscores *MBF - LAMB* at the short range.

Finally, Fig. 7 (a) shows the p_{75} when only the SMD LED strip is utilised in orange. It indicates the potential of adding the latter, were it not for the inter-strip-interference. This benefit is unfortunately limited in practice due to the LED strip's self-interference, the LEDs having a suboptimal (too directive) Lambertian order and the manifestation of LED coordinate mismatches (particularly impactful with directive LEDs). Nevertheless, close to the landing zone, approximately a decimetre accuracy is reached. Further away, due to the directivity, the SMD LEDs are only able to cover a landing range, with sufficient signal-to-noise ratio (SNR), with x and y coordinates relatively close to their x and y coordinates.

3) Commercial funnel with 2x6 LEDs: Differentiating between Fig. 7 (a) and (b) allows visualising the impact of drone funnel-induced reflections (see Fig. 1 (b)), i.e. of induced NLOS. This NLOS contribution causes *MLT*'s p_{75} to substantially shift upwards. Another, albeit smaller, p_{75}-contributing factor is the elevated dilution of precision that arose from the LEDs featuring closer together. Both effects do not (additionally) hinder *FP* or *MBF - LAMB*, due to their inherent $I_{PD,i}$-based cost function being more robust. At $82\,\text{cm}$ high, removing the SMD LED strip (the light green dot in Fig. 7 (b)) improves the p_{75} from $6.1\,\text{cm}$ to $5\,\text{cm}$, still $2.5\,\text{cm}$ inferior to when no funnel would be present.

As the $1\,\text{m}^3$ slider setup was placed in front of the funnel, Fig. 7 is also able to highlight the exponential p_{75} degradation due to noise (for a fixed gain) when the PD is further removed ($> 1\,\text{m}$). Fortunately, the presence of the funnel's guiding structures allows the landing system to be less accurate (e.g. $p_{75} \approx 10\,\text{cm}$). So even for this use case, certainly without the SMD LED strip, a combination algorithm of *MLT* and (*MBF*)

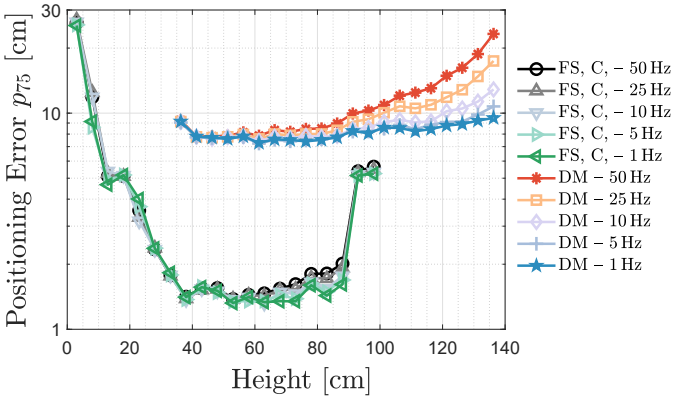

Fig. 8. Influence of averaging $I_{PD,i}$ on the measured height-p_{75} relation.

fingerprinting may do. Interestingly, when the SMD strip is present in this NLOS topology, it is better to use their $I_{PD,i}$ for positioning higher up.

4) Commercial funnel with 5 COB LEDs: Fig. 7 (b) also contains the *MLT* curve found with the drone funnel in conjunction with the 5-COB LED strip. This configuration exhibiting an inferior and superior accuracy, respectively at the nether and upper end of the measured height range, demonstrates the influence of the p_{75} on the the LEDs' placement. LED placement is thus an important parameter in maximising the VLP landing's performance.

5) Influence of Averaging: In the previous analysis, the update rate was set at $50\,\text{Hz}$. Fig. 8 visualises *MLT*'s height-p_{75} curve for the 6 COB flat surface (*FS, C*) and the double LED strip-equipped funnel (*DM*) scenario, when prior to the localisation the $I_{PD,i}$ are averaged, or equivalently, the update rate is allowed to be lowered. From Fig. 8, two conclusions can be derived: (1) averaging only entails a significant p_{75} improvement when the receiver's height increases and (2) VLP's performance at heights below $50\,\text{cm}$ is not dominated by (Gaussian) noise, but rather by bias factors.

IV. Discussion, Conclusion & Future Work

A. Discussion

As in indoor drone flight the precision landing system is only typically enabled a meter or so above the landing zone, *multilateration*-based VLP should deliver sufficiently accurate (below $3.5\,\mathrm{cm}$) positioning estimates for landing on a flat surface, equipped with a 6-element COB LED strip. The tested LED layout may seem bulky, but the previous analysis suggests it is shrinkable.

In its current form, adding a second LED strip with highly-directive LEDs, to combat positioning errors close to the landing zone, did not have the desired effect, with the main culprit being inter-LED-strip interference. The metallic surfaces of a drone funnel add a significant NLOS contribution that requires a more robust localisation.

This manuscript represents near-perpendicular landing, i.e. without the PD receiver tilting much (e.g. not more than $2°$). With tilt, the system's main performance degrading factor is highlighted. It is furthermore not easily mitigated. Other remaining challenges (to tackle) or open questions regarding the proposed landing system are:

- The extent to which errors close to the open landing zone are tolerable, as at a certain height the drone's rotors are just switched off, determines the necessity for (a) fingerprinting (hybrid).
- The present results are for one-shot VLP. Adding location robustness or filtering measures should improve the accuracy.
- Without the aid of additional sensors, the drone's yaw rotation cannot be determined.
- Though not without benefits, such as cost-reduction or near-synchronisation (but for the frequency dividers' delay), featuring the LEDs in a LED strip poses limits on the available modulation frequencies and induces the LED interference that dominates the noise profile. Both can be mitigated by improving the prototype strip's design, i.a. by adding (optical) decoupling or by modifying the frequency halver circuit that turned out to be the bandwidth-limiting factor.
- A more optimal transmitter configuration in terms of the coordinates and the radiation pattern (combination) would improve the p_{75}. A planning tool may have to incorporate NLOS effects.
- A system to accurately chart the LED coordinates is required, as mismatches (certainly for the directive LEDs) induce errors.
- (Overarching) ambient light sources do not significantly impair the positioning, as the PD (at the drone's bottom) is directed away from them, except when they induce a substantial NLOS component as a result of reflections on nearby floor patches or even on the docking station itself.

In summary, RSS-based VLP is proven to become a viable alternative for current landing systems, whose accuracies are reported to be in the $1-13\,\mathrm{cm}$ and $3.5-10\,\mathrm{cm}$ range for fusion-aided marker-based vision systems [6] and for IR-LOCK[13], respectively. Being (projected to be) more lightweight (Section IV-B) than its competitors, its potential applications are found for weight-constrained drones that do not have to lug around a camera for other purposes.

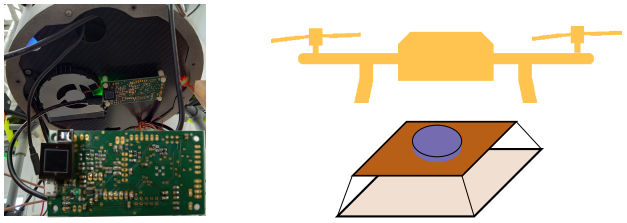

Fig. 9. (a) A photograph of the developed receiver mounted at the bottom of the drone. (b) An illustration of a future landing system.

B. Case Study: Drone-integrated VLP prototype

As the Thorlabs PDA36A2 with its power supply typically exceeds the target weight for a landing system, in the *InWareDrones* project, a cost-effective and lightweight VLP receiver prototype was also developed. It is shown mounted on a drone in Fig. 9 (a). With a partially analogue and partially digital front-end built around the Cypress Semiconductor 5LP CY8C5888LTI-LP097[14], an ARM® Cortex® - M3 CPU-based programmable System on a Chip (SoC), the photocurrent signals of one (or multiple) reverse-biased photodiode(s) (Hamamatsu Photonics' S1227-33BR and S1227-1010BR[15] in Fig. 9 (a)) are processed by various building blocks, for programmable low noise transimpedance/gain amplification, filtering, coherent analogue-to-digital conversion (ADC) and demodulation. Furthermore, a N-channel junction field-effect transistor (FET)-based bootstrapping circuit is provided for PDs with a significant junction capacitance, while the peripherals include programming headers, buttons, status LEDs, a crystal (for a stable clock), a low-dropout regulator (for supply regulation) and additional communication interfaces (I^2C, SPI, FTDI and UART).

The VLP-based receiver location estimates are computed every $100\,\mathrm{Hz}$ on an Intel® NUC®, connected via USB. (Lightweight) algorithms can be run on the receiver itself as well. The estimates are subsequently fed into a sensor fusion-based flight controller, implemented via the online asynchronous state estimation (OASE) toolbox[16] through ROS (Melodic) interfaces. These interfaces also allow querying the drone's inertial measurement unit (IMU) and/or ultra-wideband (UWB) data for input into its VLP localisation engine i.a. for tilt compensation and robustness.

C. Conclusion

This manuscript wields single photodiode-based RSS VLP for drone landing, where the transmitter infrastructure consists

[13] https://docs.px4.io/v1.9.0/en/advanced_features/precland.html
[14] https://www.cypress.com/products/32-bit-arm-cortex-m3-psoc-5lp
[15] https://www.hamamatsu.com/resources/pdf/ssd/s1227_series_kspd1036e.pdf
[16] https://www.flandersdrive.be/en/research/services/implementation-robust-reliable-localisation-systems

of a cost-effective LED strip integrated in the landing zone. 3D localisation experiments were performed with a flat surface and a commercial drone funnel. With the exception of close to the open landing zone, i.e. for receiver heights larger than $23\ \mathrm{cm}$, the coupling of multilateration (*MLT*) with a 6 COB LED strip suffices for this type of precision landing. The drone funnel's induced NLOS diminishes the *MLT* accuracy in the practical range, pushing it towards a decimetre. In both configurations, manual fingerprinting demonstrates VLP's viability to cover ranges up to $1\ \mathrm{m}$ above the landing zone, and more. Finally, the aptitude of VLP for drone landing was demonstrated by showcasing the developed drone-integrated VLP solution.

D. Future Work

The future work of the VLP-based landing system mainly entails both reducing the positioning error, certainly in case of significant receiver tilt, and deriving the lightweight prototype's accuracy with comparable measurements. In addition, instead of relying on an IMU [19], utilising a VLP receiver that consists of a single PD with a nonzero angle of inclination or that is based on multiple PDs [20] will allow to unambiguously determine the drone's yaw (with respect to the landing platform). As mentioned in the discussion (Section IV-A), the optimal LED configuration needs to be determined as well, thereby considering NLOS and the available degrees of freedom (e.g. LEDs in/on the funnel's sides instead of its bottom plate). Other designations for the developed (sub)systems are also envisioned.

1) Different Landing Configurations: The solution can also feature for landing on a square/circular frustum that accommodates the drone's legs along its mantel (Fig. 9 (b) illustrates). This configuration results in an excellent 3D charging coil alignment for wireless power transfer, when the charging coils are located on top of the frustum and at the bottom of the drone.

2) Applications of the modulated LED strip: The modulated (SMD) strip principle, with visible or even infrared LED, can also serve for i.a. (a) the safe autonomic drone navigation in very tight spaces/corridors with a longitudinally placed strip, (b) the precise picking-up of goods from storage racks that are equipped with the LED modules, (c) localisation where LED strips are already present, such as in the handrails or staircases found in e.g. tunnels or caves, and (d) the cost-effective modulation of a part of a LED armature where (groups of) LEDs are already serially addressed.

References

[1] S. Sarkar, M. W. Totaro and A. Kumar, "An Intelligent Framework for Prediction of a UAV's Flight Time," *16th International Conference on Distributed Computing in Sensor Systems (DCOSS)*, Marina del Rey, CA, USA, 2020, pp. 328–332, doi: 10.1109/DCOSS49796.2020.00058.

[2] T. Campi, S. Cruciani and M. Feliziano, "Wireless Power Transfer Technology Applied to an Autonomous Electric UAV with a Small Secondary Coil," in *Energies*, vol. 11, no. 352, pp. 1–15, 2018, doi: 10.3390/en11020352.

[3] K. Fujii, K. Higuchi and J. Rekimoto, "Endless Flyer: A Continuous Flying Drone with Automatic Battery Replacement," *IEEE 10th International Conference on Ubiquitous Intelligence and Computing and IEEE 10th International Conference on Autonomic and Trusted Computing*, Vietri sul Mare, Italy, 2013, pp. 216–223, doi: 10.1109/UIC-ATC.2013.103.

[4] C. H. Choi, H. J. Jang, S. G. Lim, H. C. Lim, S. H. Cho and I. Gaponov, "Automatic Wireless Drone Charging Station," *International Conference on Control, Automation and Information Sciences (ICCAIS)*, Ansan, Korea, 2016, pp. 132-136, doi: 10.1109/ICCAIS.2016.7822448.

[5] H. Tanaka and Y. Matsumoto, "Autonomous Drone Guidance and Landing System Using AR/high-accuracy Hybrid Markers," *IEEE 8th Global Conference on Consumer Electronics (GCCE)*, Osaka, Japan, 2019, pp. 598–599, doi: 10.1109/GCCE46687.2019.9015373.

[6] J. Wubben, F. Fabra, C. T. Calafate, T. Krzeszowski, J. M. Marquez-Barja, J.-C. Cano and P. Manzoni, "Accurate Landing of Unmanned Aerial Vehicles Using Ground Pattern Recognition," in *Electronics*, vol. 8, no. 1532, pp. 1–16, 2019, doi: 10.3390/electronics8121532.

[7] A. Al-Kaff, D. Martín, F. García, A. de la Escalera, J. M. Armingol, "Survey of computer vision algorithms and applications for unmanned aerial vehicles," in *Expert Systems with Applications*, vol. 92, pp. 447–463, 2018, doi: 10.1016/j.eswa.2017.09.033.

[8] J. Janousek and P. Marcon, "Precision landing options in unmanned aerial vehicles," *International Interdisciplinary PhD Workshop (IIPhDW)*, Świnoujście, Poland, 2018, pp. 58–60, doi: 10.1109/IIPHDW.2018.8388325.

[9] N. Xuan-Mung, S. K. Hong, N. P. Nguyen, L. N. N. T. Ha and T. -L. Le, "Autonomous Quadcopter Precision Landing Onto a Heaving Platform: New Method and Experiment," in *IEEE Access*, vol. 8, pp. 167192–167202, 2020, doi: 10.1109/ACCESS.2020.3022881.

[10] B. M. M. Rahman, T. Li and Y. Wang, "Recent Advances in Indoor Localization via Visible Lights: A Survey," in *Sensors*, vol. 20, no. 1382, 2020, doi: 10.3390/s20051382.

[11] Y. Zhuang, L. Hua, L. Qi, J. Yang, P. Cao, Y. Cao, Y. Wu, J. Thompson and H. Haas, "A Survey of Positioning Systems Using Visible LED Lights," in *IEEE Communications Surveys & Tutorials*, vol. 20, no. 3, pp. 1963–1988, 2018, doi: 10.1109/COMST.2018.2806558.

[12] Y. Almadani, D. Plets, S. Bastiaens, W. Joseph, M. Ijaz, Z. Ghassemlooy and S. Rajbhandari, "Visible Light Communications for Industrial Applications - Challenges and Potentials," in *Electronics*, vol. 9, no. 12, pp. 1–38, 2020, doi: 10.3390/electronics9122157.

[13] S. De Lausnay, L. De Strycker, J. Goemaere, N. Stevens and B. Nauwelaers, "A Visible Light Positioning system using Frequency Division Multiple Access with square waves," *9th International Conference on Signal Processing and Communication Systems (ICSPCS)*, Cairns, Australia, 2015, pp. 1-7, doi: 10.1109/ICSPCS.2015.7391787.

[14] S. Bastiaens, K. Deprez, L. Martens, W. Joseph and D. Plets, "A Comprehensive Study on Light Signals of Opportunity for Subdecimetre Unmodulated Visible Light Positioning," in *Sensors*, vol. 20, no. 19, pp. 1–27, 2020, doi:10.3390/s20195596.

[15] M. Kahn and J. R. Barry, "Wireless infrared communications," in *Proceedings of the IEEE*, vol. 85, pp. 265–298, 1997, doi: 10.1109/5.554222.

[16] D. Plets, Y. Almadani, S. Bastiaens, M. Ijaz, L. Martens and W. Joseph, "Efficient 3D Trilateration Algorithm for Visible Light Positioning," in *Journal of Optics*, vol. 21, no. 5, pp. 1–4, 2019, doi: 10.1088/2040-8986/ab1389.

[17] S. Bastiaens, D. Plets, L. Martens and W. Joseph, "Impact of Non-ideal LED Modulation on RSS-based VLP Performance," *IEEE 29th Annual International Symposium on Personal, Indoor and Mobile Radio Communications (PIMRC)*, Bologna, Italy, 2018, pp. 1–5, doi: 10.1109/PIMRC.2018.8581009.

[18] T. Komine and M. Nakagawa, "Fundamental analysis for visible-light communication system using LED lights," in *IEEE Transactions on Consumer Electronics*, vol. 50, no. 1, pp. 100–107, 2004, doi: 10.1109/TCE.2004.1277847.

[19] M. Yasir, S. Ho and B. N. Vellambi, "Indoor Positioning System Using Visible Light and Accelerometer," in *Journal of Lightwave Technology*, vol. 32, no. 19, pp. 3306–3316, 2014, doi: 10.1109/JLT.2014.2344772.

[20] S. Shen, S. Li and H. Steendam, "Simultaneous Position and Orientation Estimation for Visible Light Systems With Multiple LEDs and Multiple PDs," in *IEEE Journal on Selected Areas in Communications*, vol. 38, no. 8, pp. 1866–1879, 2020, doi: 10.1109/JSAC.2020.3000805.